# Self-Assembly of a Rare High Spin FeII/PdII Tetradecanuclear Cubic Cage Constructed via the Metalloligand Approach

Hyunsung Min [1], Alexander R. Craze [1,2], Takahiro Taira [3], Matthew J. Wallis [1], Mohan M. Bhadbhade [4], Ruoming Tian [4], Daniel J. Fanna [5], Richard Wuhrer [5], Shinya Hayami [3], Jack K. Clegg [6], Christopher E. Marjo [4], Leonard F. Lindoy [7] and Feng Li [1,*]

[1] School of Science, Western Sydney University, Locked Bag 1797, Penrith, NSW 2751, Australia; 17792947@student.westernsydney.edu.au (H.M.); alexander.craze@chem.ox.ac.uk (A.R.C.); 17232236@student.westernsydney.edu.au (M.J.W.)
[2] Department of Chemistry, University of Oxford, 12 Marsfied Road, Oxford OX1 3TA, UK
[3] Department of Chemistry, Graduate School of Science and Technology, Kumamoto University, 2-39-1 Kurokami, Chuo-ku, Kumamoto 860-8555, Japan; 215d8108@st.kumamoto-u.ac.jp (T.T.); hayami@kumamoto-u.ac.jp (S.H.)
[4] Mark Wainwright Analytical Centre, University of New South Wales, Kensington, NSW 2052, Australia; m.bhadbhade@unsw.edu.au (M.M.B.); r.tian@unsw.edu.au (R.T.); c.marjo@unsw.edu.au (C.E.M.)
[5] Advanced Materials Characterisation Facility, Western Sydney University, Locked Bag 1797, Penrith, NSW 2751, Australia; d.fanna@westernsydney.edu.au (D.J.F.); richard.wuhrer@westernsydney.edu.au (R.W.)
[6] School of Chemistry and Molecular Bioscience, The University of Queensland, St Lucia, QLD 4072, Australia; j.clegg@uq.edu.au
[7] School of Chemistry, University of Sydney, Camperdown, NSW 2006, Australia; leonard.lindoy@sydney.edu.au
* Correspondence: feng.li@westernsydney.edu.au; Tel.: +61-2-9685-9987

**Abstract:** Polynuclear heterobimetallic coordination cages in which different metal cations are connected within a ligand scaffold are known to adopt a variety of polyhedral architectures, many of which display interesting functions. Within the extensive array of coordination cages incorporating Fe(II) centres reported so far, the majority contain low-spin (LS) Fe(II), with high-spin (HS) Fe(II) being less common. Herein, we present the synthesis and characterisation of a new tetradecanuclear heterobimetallic $[Fe_8Pd_6L_8](BF_4)_{28}$ (**1**) cubic cage utilising the metalloligand approach. Use of the tripodal tris-imidazolimine derivative (**2**) permitted the formation of the tripodal HS Fe(II) metalloligand $[FeL](BF_4)_2 \cdot CH_3OH$ (**3**) that was subsequently used to form the coordination cage **1**. Magnetic and structural analyses gave insight into the manner in which the HS environment of the metalloligand was transferred into the cage architecture along with the structural changes that accompanied its occupancy of the eight corners of the discrete cubic structure.

**Keywords:** cubic cage; metalloligand; tripodal ligand; heterobimetallic

## 1. Introduction

In recent years, the self-assembly of polyhedral materials that incorporate large internal cavities has attracted increasing attention, as they have demonstrated potential for applications involving molecular sensing, guest uptake and release, catalysis, the stabilisation of reactive species and the generation of magnetic materials [1–6]. The structural diversity and complexity of available coordination cages are continually being extended, underpinned by several key stratagems for achieving self-assembly. Some prominent synthetic strategies utilised to create such materials include the metalloligand approach, [7,8] the symmetry interaction approach, [9] the molecular panelling approach, [10] the subcomponent self-assembly approach [11] and the molecular library approach [12,13]. These approaches exploit the symmetry and coordination directions of molecular components in order to influence their predisposition to self-assemble into larger, more complex architectures. The metalloligand strategy employs multifunctional metalloligands with well-defined

geometrical and electronic preferences to allow for the rational design and synthesis of multifunctional/heteronuclear cages with a wide variety of predefined topologies [7,8]. Careful selection of a secondary coordination site (or sites), separate from the coordination sphere of the metalloligand and therefore free to coordinate to a second metal centre, makes the generation of specific self-assembled geometries possible. Using the above approaches has resulted in the report of a wide variety of metallosupramolecular cages, demonstrating a range of behaviours arising from their host−guest, redox, photo-active and magnetic properties [1,2,14–19]. Much of this research has focused on homometallic cage motifs.

In the search for increased complexity and function, there has been growing interest in heterometallic cage systems. Stratagems such as the metalloligand approach and the use of self-assembly, or ones based on the hard or soft nature of the metal cations and ligand donors, as well as on the preferred geometry of individual metal centres can be utilised to design more complex structures incorporating multiple metal centres with different identities and functions [1,2,7,8,18,19]. The presence of two different metal cations in a discrete cage structure potentially provides access to new structural motifs, geometries and functions, with more complex self-sorting achievable through the presence of the two metal centres with different bonding affinities and/or preferred geometries [1,2,7,8,18,19].

Spin crossover (SCO) is another phenomenon continuing to display very widespread interest [20,21]. To date, a plethora of coordination cages incorporating Fe(II) that display an array of geometries have been reported [1,2,7,8,22–24]. The majority of these contain low-spin (LS) Fe(II) centres, while high-spin (HS) cages have been less reported [2,23]. For instance, the first Fe(II) cage exhibiting SCO was reported as recently as 2009 [25]. Typically, the LS cages have been designed using ligands based on pyridylimine and 2,2′-bipyiridyl precursors [11,18]. The synthesis of spin-switching Fe(II) cages relies on the design of a weaker ligand field, and as such, the majority of SCO Fe(II) cages utilise ligands incorporating the imidazolimine functional group [2,22,23,26,27]. Upon self-assembly, the spin-state of the metal centres in a cage can be manipulated by both steric and electronic variations in the chosen ligands. It has been well demonstrated that even small variations of a ligand's electronic nature can cause dramatic changes in the SCO of the resultant cage structure [22–30].

Recently, there has been a growing number of reported heterobimetallic cages that exhibit SCO. These represent a variety of new and complex structures with interesting functions [2]. The first SCO $Fe(II)_8M_6$ cage was reported by Lützen and coworkers in 2017, utilising a porphyrin-based imdazolimine ligand [27]. On the other hand, Fe(II) cubic cages that remain HS have been reported by our group [31] and others [32–34]. The former HS cage [31] employed a weaker field ligand incorporating both pyridyl and pyrazole donors (that is, the 1,5-bis((3-(pyridin-2-yl)-1H-pyrazol-1-yl)methyl)naphthalene ligand). However, Lützen, Nitschke and Hooley induced steric strain in the pyridyl-derived structure, which acted to stabilise the Fe(II) centres in their HS state [32–34].

In this work, we have manipulated the ligand field of the well-studied tris(2,4-imidazolimine) coordination environment [35–37], which has been shown to result in Fe(II) SCO in most cases. We modified the ligand field through the addition of three 4-pyridyl groups (Figure 1) to yield (**2**), which resulted in HS Fe(II) centres in the metalloligand $FeL(BF_4)_2$. (**3**) This metalloligand, in turn, gave rise to the self-assembled $[Fe_8Pd_6L_8](BF_4)_{28}$ octahedral cage (**1**) (Scheme 1). Thus, both an HS metalloligand and a HS heterobimetallic cage were successfully synthesised.

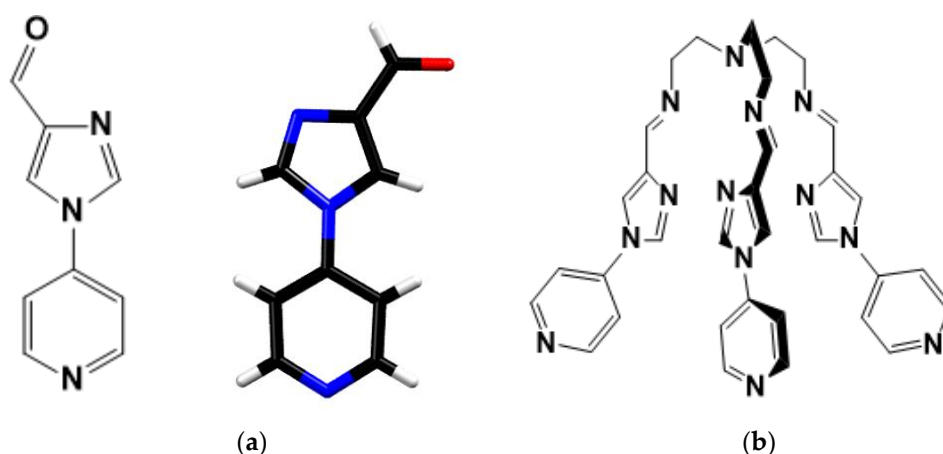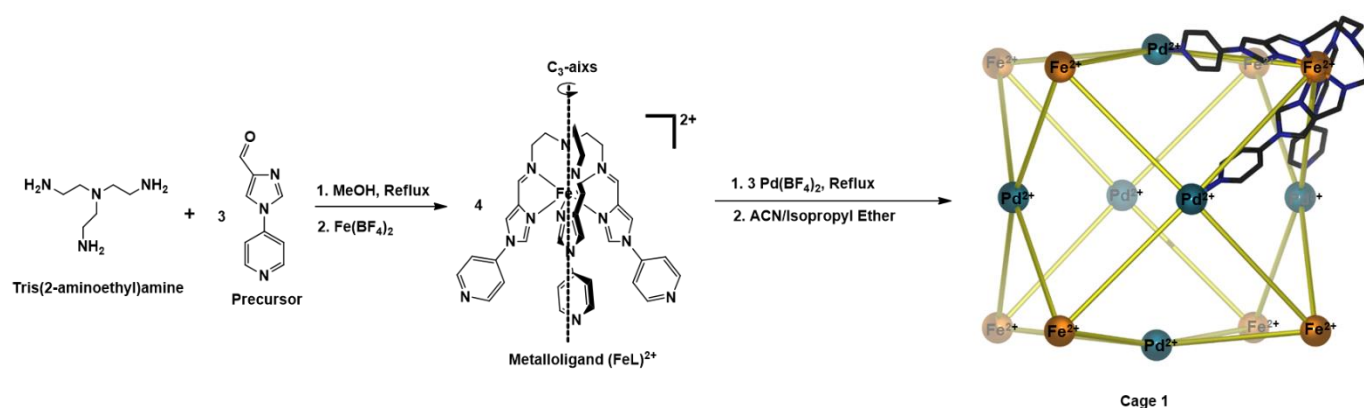**Figure 1.** (**a**) Molecular structure of the precursor with its crystal structure, Colour codes: C-Black, N-blue, O-Red, H-White (**b**) Molecular structure of tripodal ligand **2**.



**Scheme 1.** Synthesis of cubic cage **1** using the metalloligand approach.

## 2. Materials and Methods

### 2.1. MS, NMR, SEM, EDS and X-ray Mapping Measurements

High resolution ESI−MS data were acquired using a Waters Xevo QToF mass spectrometer (Waters, Milford, MA, USA), operating in positive ion mode. Samples were dissolved in MeCN and infused directly into the ESI source via syringe.

Nuclear Magnetic Resonance (NMR) experiments were performed on an Oxford/Varian Mercury 300 MHz NMR, operating with VnmrJ Version 4.2 Revision A software and equipped with a Varian 300AutoSW PFT probe at Biomedical Magnetic Resonance Facility (Western Sydney University). CHN analyses was carried out at Kumamoto University, Japan.

Scanning Electron Microscopy (SEM) and Energy Dispersive Spectroscopy (EDS) spot analysis were acquired using a Jeol 6510LV SEM in low vacuum with a chamber pressure of 30 Pa and an accelerating voltage of 25 kV. Samples were mounted to an aluminium stub with double-sided conductive carbon tape and then imaged uncoated. Spot EDS analysis was carried out using Moran Scientific microanalysis software with a silicone Drift Detector (SDD). X-ray mapping was carried out using a Hitachi FlexSEM1000II SEM fitted with a Bruker EDS microanalysis system. Samples were mounted on a silicone wafer and analysed in high vacuum uncoated. Elemental maps were pseudo-coloured to assist in the visual clarity of element distribution.

### 2.2. Magnetic Measurements

Susceptibility data were collected using a Quantum Design SQUID magnetometer (Quantum Design, San Diego, CA, USA) calibrated against a standard palladium sample. The data was collected between 10 and 300 K and cycled from 300 → 10 → 300 K. The scan

rate was fixed at 2 K min$^{-1}$. Measurements were taken continuously under an applied field of 0.5 T.

### 2.3. Single Crystal X-ray Diffraction Measurements

All single crystal data was collected from the MX1 beamline at the Australian Synchrotron using silicon double crystal monochromated radiation (λ = 0.71073 Å) at 100 K [38]. At the Australian synchrotron beamline, the XDS software [39] was used for data integration, processing and scaling. The empirical absorption correction was then applied at the synchrotron using SADABS [40]. The structure was solved by ShelXT [41] using the intrinsic phasing method and the full-matrix least-squares refinements were carried out using a suite of SHELX programs [42,43] via the Olex2 interface [44]. Non-hydrogen atoms were refined anisotropically for the precursor and the metalloligand, however, only the coordinating nitrogens and the heavy metal (Fe and Pd) atoms were refined anisotropically due to low resolution data. Hydrogen atoms were included in idealized positions and refined using a riding model. The crystallographic data (Table 1) in CIF format has been deposited at the Cambridge Crystallographic Data Centre with CCDC nos. 2170053, 2170063 and 2170771. It is available free of charge from the Cambridge Crystallographic Data Centre, 12 Union Road, Cambridge CB2 1 EZ, UK; fax: (+44) 1223-336-033; or e-mail: deposit@ccdc.cam.ac.uk. Crystal of **1** diffracted essentially only to lower angles of theta and, therefore, the data for **1** was collected at low resolution (~1.00 Å).

**Table 1.** Crystallographic data for 1-(pyridine-4-yl)-1H-imidazole-4-carbaldehyde, FeL(BF$_4$)$_2$ (**3**) and Heterobimetallic cage (**1**).

| Compound | 1-(pyridine-4-yl)-1H-imidazole-4-carbaldehyde | FeL(BF$_4$)$_2$.CH$_3$OH (3) | Cage (1) |
|---|---|---|---|
| CCDC Number | 2170053 | 2170063 | 2170771 |
| Empirical formula | C$_9$H$_7$N$_3$O | C$_{34}$H$_{37}$B$_2$F$_8$FeN$_{13}$O | C$_{276}$H$_{282}$B$_{28}$F$_{112}$Fe$_8$N$_{110}$OPd$_6$ |
| Formula weight | 173.18 | 873.23 | 8671.98 |
| Temperature/K | 100 | 100 | 100 |
| Crystal system | Monoclinic | Monoclinic | Cubic |
| Space group | P2$_1$/c | P2$_1$/c | Fm-3c |
| a/Å | 3.6800 (7) | 11.565 (2) | 46.361 (5) |
| b/Å | 22.050 (4) | 15.555 (3) | 46.361 (5) |
| c/Å | 9.6300 (19) | 21.169 (4) | 46.361 (5) |
| α/° | 90 | 90 | 90 |
| β/° | 99.41 (3) | 91.87 (3) | 90 |
| γ/° | 90 | 90 | 90 |
| Volume/Å$^3$ | 770.9 (3) | 3806.1 (13) | 99,643 (35) |
| Z | 4 | 4 | 8 |
| ρ$_{calc}$g/cm$^3$ | 1.492 | 1.524 | 1.156 |
| μ/mm$^{-1}$ | 0.103 | 0.485 | 0.526 |
| F(000) | 360 | 1792 | 34784 |
| Crystal size/mm$^3$ | 0.2 × 0.02 × 0.02 | 0.02 × 0.02 × 0.01 | 0.2 × 0.2 × 0.2 |
| Radiation/Å | MoKα (λ = 0.71073) | MoKα (λ = 0.71073) | MoKα (λ = 0.71073) |
| 2Θ range for data collection/° | 3.694 to 52.744 | 3.25 to 57.062 | 4.304 to 34.444 |
| Index ranges | −4 ≤ h ≤ 4, −27 ≤ k ≤ 27, −11 ≤ l ≤ 11 | −12 ≤ h ≤ 12, −18 ≤ k ≤ 18, −24 ≤ l ≤ 24 | −38 ≤ h ≤ 38, −38 ≤ k ≤ 38, −38 ≤ l ≤ 38 |
| Reflections collected | 16,679 | 47,189 | 96,862 |
| Independent reflections | 16,679 [R$_{int}$ = 0.1048, R$_{sigma}$ = 0.1185] | 7210 [R$_{int}$ = 0.0239, R$_{sigma}$ = 0.0134] | 1343 [R$_{int}$ = 0.1650, R$_{sigma}$ = 0.0174] |
| Data/restraints/parameters | 16,679/0/119 | 7210/0/534 | 1343/46/125 |
| Goodness-of-fit on F$^2$ | 1.13 | 1.04 | 1.814 |
| Final R indexes [I > = 2σ (I)] | R$_1$ = 0.0782, wR$_2$ = 0.2147 | R$_1$ = 0.0274, wR$_2$ = 0.0710 | R$_1$ = 0.1323, wR$_2$ = 0.3998 |
| Final R indexes [all data] | R$_1$ = 0.1222, wR$_2$ = 0.2889 | R$_1$ = 0.0277, wR$_2$ = 0.0712 | R$_1$ = 0.1525, wR$_2$ = 0.4268 |
| Largest diff. peak/hole/e Å$^{-3}$ | 0.42/−0.62 | 0.57/−0.39 | 1.83/−0.46 |

In total, there are eight BF$_4^-$ anions encapsulated inside the cage and twenty BF$_4^-$ anions seen outside of the cage. The two outer BF$_4^-$ in the asymmetric unit were given $^5/_6$ occupancy to satisfy the chemical formula, but these occupancies may have some variation in reality. The reason for the selection of the outer two BF$_4^-$ anions for the reduction of

occupancies was due to their larger Uiso compared to the inner $BF_4^-$ anions encapsulated in the cage. The solvent mask found a residual electron density of 41 electrons, which may be attributed to solvent or partially occupied solvents. Only the heavy atoms (Fe, Pd) and their coordinating nitrogens were refined anisotropically with other non-hydrogen atoms refined isotropically. The anions were restrained using SADI and RIGU, while the solvent was restrained with DIFX and RIGU. Furthermore, the coordinating nitrogens of the cage (N3, N4 and N5) were restrained with RIGU. The final R factors were in the range (0.13) and the other refinement parameters (wR2, GooF) were in acceptable ranges for the asymmetric unit in the cubic space group (Table 1).

### 2.4. General Synthetic Procedures

Synthesis of 1-(pyridine-4-yl)-1*H*-imidazole-4-carbaldehyde. The procedure was adapted from a literature synthesis [45]. 4-Brompyridine hydrochloride (779.1 mg, 4.01 mmol) was mixed with 4-imidazolecarboxaldehyde (541.2 mg, 5.63 mmol, excess), cesium carbonate (2.6 g, 8.0 mmol) and copper(I) iodide (152.8 mg, 0.80 mmol) in 8 mL of dimethylformamide. The flask was evacuated and back-filled with $N_2$ three times, then heated at 120 °C for 48 h. The resulting brown mixture was allowed to cool, diluted with ethyl acetate (6 mL) and filtered through a plug of celite. The mixture was washed three times with 20 mL ethyl acetate and the resulting brown solution was concentrated to 30 mL for purification via column chromatography (10:1 ethyl acetate/methanol eluent). The yellow solution was evaporated to desiccation and the product was recrystallised from ethanol to give white crystals. Yield: 258 mg, 36.8%. $^1$H NMR (DMSO-d$_6$, 300 MHz) δ (ppm); 9.84 (s, 1H), 8.86 (s, 1H), 8.75 (s, 3H), 7.88 (d, 2H); $^{13}$C NMR (DMSO-d$_6$, 75 MHz) δ (ppm); 186.01, 151.97, 143.18, 142.82, 138.29, 125.30, 114.96.

Synthesis of ligand (**2**). Tris(2-aminoethyl)amine (108.9 mg, 0.74 mmol) in 10 mL acetonitrile (MeCN) was added to a solution of 1-(pyridine-4-yl)-1*H*-imidazole-4-carbaldehyde (403.7 mg, 2.33 mmol) in 10 mL of MeCN. The reaction mixture was heated at reflux while stirring for 3 h and then the pale white precipitate that formed was collected by filtration and washed with cold MeCN (3 × 5 mL) to give a white powder. Yield: 382 mg, 80.45%. $^1$H NMR (CDCl$_3$, 300 MHz) δ (ppm); 8.725 (d, 2H), 8.260 (s, 1H), 7.972 (s, 1H), 7.883 (s, 1H), 7.397 (d, 2H), 3.720 (t, 2H), 2.910 (t, 2H); $^{13}$C NMR (CDCl$_3$, 75 MHz) δ (ppm); 155.85, 151.82, 143.11, 142.40, 116.23, 114.36, 60.04, 55.43.

Synthesis of Metalloligand FeL(BF$_4$)$_2$ (**3**). Method 1: Tris(2-aminoethyl)amine (205.5 mg, 1.41 mmol) in 10 mL of methanol (MeOH) was added to a solution of 1-(pyridine-4-yl)-1*H*-imidazole-4-carbaldehyde (730.1 mg, 4.22 mmol) in 15 mL of methanol. The reaction mixture was heated at reflux with stirring for 3 h leading to a clear pale yellow solution. After cooling the solution, iron(II) tetrafluoroborate hexahydrate (474.4 mg, 1.41 mmol) in 10 mL of methanol was added dropwise to the reaction mixture while stirring. The mixture was then refluxed for a further 1 h, leading to an orange solution. The solution was left to cool. Slow evaporation of the reaction mixture resulted in orange crystals. The orange crystals of FeL(BF$_4$)$_2$ were isolated by filtration and washed with cold methanol, then allowed to dry in air. Yield: 801 mg, 67.7%.

Method 2: Iron(II) tetrafluoroborate hexahydrate (174.3 mg, 0.52 mmol) in methanol (10 mL) was added dropwise into a solution of **2** (301.6 mg, 0.49 mmol) in methanol (10 mL). The reaction mixture was heated at reflux for 1 h. The resulting orange solution was left to slowly evaporate. The orange crystals of FeL(BF$_4$)$_2$ that formed were isolated by filtration and washed with cold methanol. Yield: 254 mg, 61.2%.

Elemental analysis (%) (calculated for C$_{33}$H$_{33}$N$_{13}$FeB$_2$F$_4$·CH$_3$OH): C (46.77, 46.26), H (4.27, 4.27), N (20.85, 20.57); HR-ESI MS (positive ion detection, MeCN): $m/z$ = [FeL(BF$_4$)]$^{1+}$; 754.2412 [FeL]$^{2+}$; 333.6189; a single crystal obtained by method 1 was used for the single crystal X-ray study.

Synthesis of Heterobimetallic Cage (**1**). Tetrakis(acetonitrile)palladium(II) tetrafluoroborate (63.5 mg, 0.14 mmol) in MeCN (10 mL) was added dropwise to FeL(BF$_4$)$_2$ (160.3 mg, 0.19 mmol) in MeCN (10 mL). The reaction mixture was heated at reflux while stirring

for 1 h, leading to a clear orange solution. The orange solution was slowly diffused with di-isopropyl ether which led to the formation of orange cubic crystals of **1**. Yield: 41 mg (based on palladium), 20.8%; HR−ESI MS (positive ion detection, MeCN): $m/z$ = 964.0559 $\{[Fe_8Pd_6L_8](BF_4)_{20}\}^{8+}$.

## 3. Results and Discussion

### 3.1. Characterisation of Ligand (2) and Its Precursor

The $^1H$ NMR and $^{13}C$ NMR (Figures S1–S4) confirmed the formation of the precursor (1-(pyridine-4-yl)-1*H*-imidazole-4-carbaldehyde) and ligand (**2**). X-ray quality crystals of the precursor (Figure 1a) were obtained through the slow evaporation of the precursor in ethanol, and crystallographic data were collected at 100 K. The precursor crystallises in monoclinic space group $P2_1/c$ with four precursor moieties per unit cell.

### 3.2. Characterisation of Fe(II) Metalloligand (3)

The high-resolution ESI−MS of Fe(II) metalloligand (**3**) identfied $m/z$ values at 333.6085 and 754.2412, which corresponds to $[FeL]^{2+}$ and $[FeL(BF_4)]^{1+}$ (L= **2**), respectively (Figures S5–S7).The isotopic pattern of both charged species of the metalloligand is in good agreement with their simulated isotopic distribution.

X-ray quality crystals were obtained through the slow evaporation of $FeL(BF_4)_2$ solution in methanol; crystallographic data were collected at 100 K. Single crystal X-ray diffraction confirmed the formation of metalloligand $FeL(BF_4)_2$ (Figure 2). $FeL(BF_4)_2$ crystallises in the monoclinic space group $P2_1/c$ with a single metalloligand in the asymmetric unit. The six imidazolimine nitrogen donor atoms of the tripodal L form an octahedral coordination sphere surrounding the central Fe(II) metal centre. The average Fe-N bond lengths of 2.20 Å, as well as the angular distortion parameter Σ value of 105°, are consistent with the HS Fe(II) complexes (Table 2). This is confirmed by magnetic susceptibility measurements (Figure 3) that exhibit a HS character over the range of 300–45 K, with a room temperature $\chi_M T$ of 3.8 $cm^3Kmol^{-1}$, that is consistent with a single Fe(II) center (S = 2) being in the HS $^5T_2$ state. Below 45 K, the observed decrease in $\chi_M T$ is attributed to zero-field-splitting in the Fe(II) centers. This is confirmed in the plot of $\chi_M^{-1}$ versus *T* (Figure 3a) that demonstrates a linear Curie−Weiss relationship that is indicative of paramagnetic behaviour.
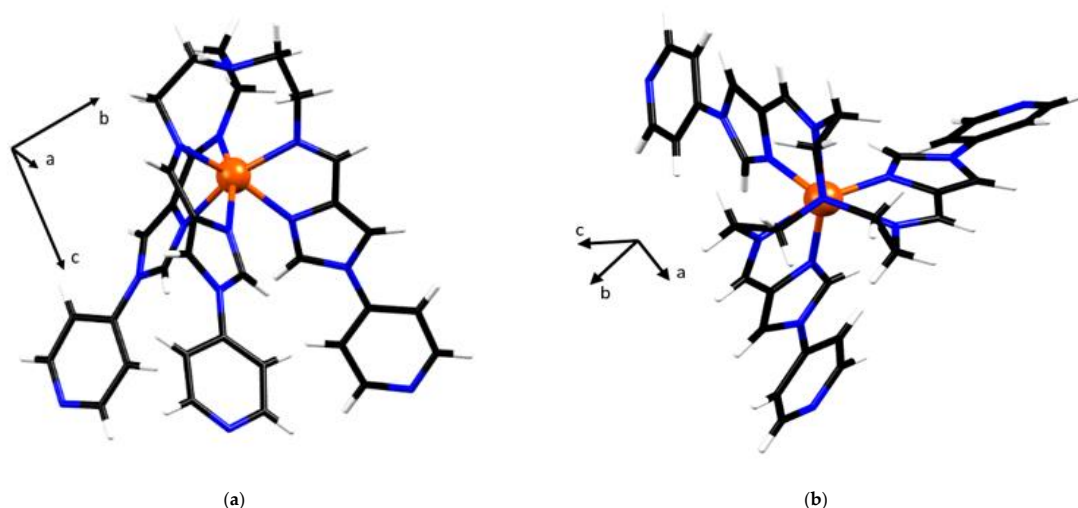


(a)                                    (b)

**Figure 2.** Crystal structure of the metalloligand $FeL^{2+}$. Colour codes: Fe, orange; C, black; N, blue; H, white. Solvent and anions are not shown. (**a**) Single crystal structure of (lambda) metalloligand $FeL^{2+}$. (side view), and (**b**) metalloligand $FeL^{2+}$. Viewed down the $C_3$ axis. The cell direction vectors are to scale with the cell parameters in each projection.

**Table 2.** Comparison of octahedral distortion parameters and average Fe-N bond lengths in FeL(BF$_4$)$_2$ (**3**) and the heterobimetallic cage (**1**).

| Compound | Average Fe(II)-N Bond Length (Å) | $\zeta$ (Å) | $\delta$ | $\Sigma$ (Degrees) | $\Theta$ (Degrees) |
|---|---|---|---|---|---|
| FeL(BF$_4$)$_2$ (100K) | 2.20 | 0.16 | 0.00018 | 105.0 | 280.4 |
| 1 (100K) | 2.19 | 0.11 | 0.000066 | 131.3 | 374.1 |



(a)           (b)
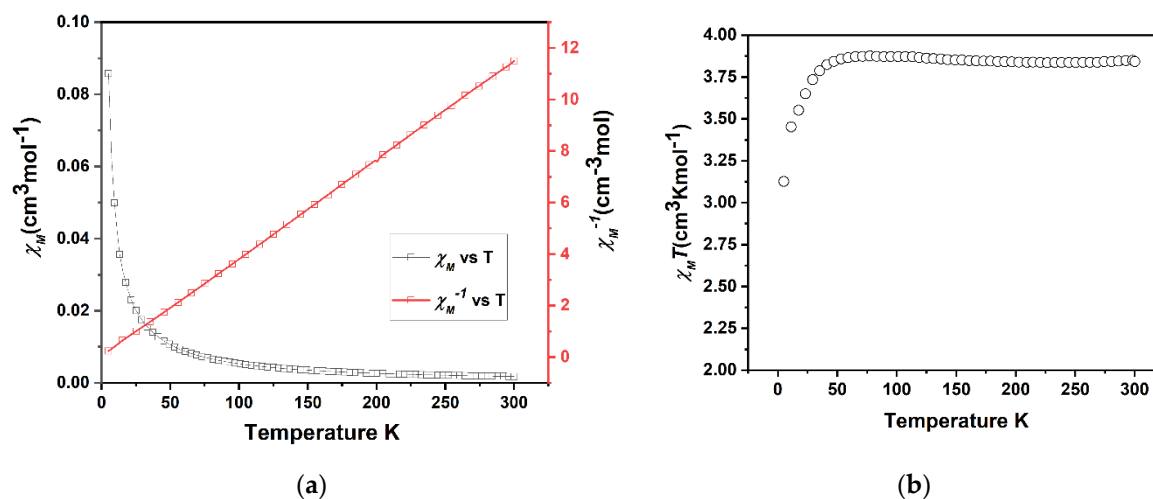
**Figure 3.** (**a**) A combined plot of the molar magnetic susceptibility ($\chi_M$) and inverse magnetic susceptibility ($\chi_M{}^{-1}$) of FeL(BF$_4$)$_2$ (**3**) against temperature. (**b**) A plot of the magnetic susceptibility ($\chi_M T$) vs. T per metalloligand. Both plots are indicative of the presence of HS (paramagnetic) Fe(II).

The metalloligand (**3**) exists in the two enantiomeric configurations $\delta$ (clockwise) or $\Lambda$ (anticlockwise), resulting from the screw sense of the ligand arrangement of tripodal L around the Fe(II) metal centre. In the asymmetric unit FeL(BF$_4$)$_2$ crystallises with two tetrafluoroborate anions, in keeping with the charge state of Fe(II) and a single methanol solvent molecule. Hydrogen bonding (B1-F4···H6B, B2-F7···H7A and MeOH···N4A-L) involving the anions and the ethanol molecule is present, with the methanol molecule and the tetrafluoroborate anions being involved in two and three hydrogen bonds with the metalloligand, respectively.

### 3.3. Characterization of the Coordination Cage [Fe$_8$Pd$_6$L$_8$]$^{28+}$

An optical microscope image and the scanning electron microscopy (SEM) photograph indicated that crystalline **1** undergoes rapid decay upon losing its solvent (Figure 4). In addition, scanning electron microscopy/energy-dispersive spectroscopy (SEM−EDS) analysis of cage **1** confirmed that the ratio of Fe(II) to Pd(II) in the cage is approximately 4:3 (Figure 4). Additionally, the EDS results confirmed the presence of C, N, F, Fe and Pd; the element maps indicated that each element was uniformly distributed as well as being chemically homogeneous (Figure 4).

The high-resolution ESI−MS showed *m/z* peaks at 613.8661, 677.5752, 754.0326, 847.4875, 964.0559, 114.3608, 1314.9109 and 1595.4788, which correspond to stepwise loss of twelve, eleven, ten, nine, eight, seven, six and five BF$_4{}^-$ anions, respectively. The expected isotopic patterns for the eight charged species (Figure S8) were also observed, with the calculated patterns being in good agreement with their isotopic distribution.
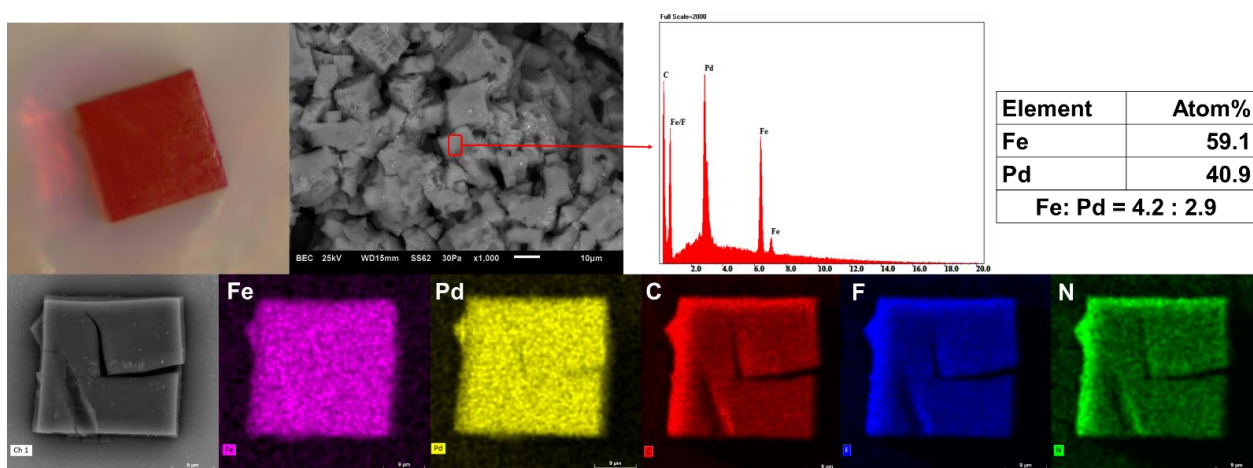
**Figure 4.** A crystal of cage **1** shown as an optical microscope image (Top left); a backscattering SEM image (Top middle left); corresponding EDS analysis results (Top middle right); atomic ratio of Fe and Pd (Top right); a backscattering SEM image of a single crystal of cage **1** (Bottom left); and X-ray mapping (Bottom). The EDS spectrum confirms an atomic ratio of Fe:Pd $\approx$ 4:3. The X-ray mapping results for each element (Fe: pink, Pd: yellow, C: red, F: blue and N: green) demonstrate that the respective elements are chemically homogeneous.

The single crystal X-ray structure determination at 100 K confirmed the heterobimetallic cage structure of **1**. The cage crystallised in the space group *Fm*-3*c*, with the asymmetric unit containing one third of one ligand, one iron(II) ion and one palladium(II) ion. Eight tetrafluoroborate ($BF_4^-$) anions are encapsulated in the cage void, which has a guest accessible volume of 41 Å$^3$ (Figure 5) and an additional twenty $BF_4^-$ ions shared across two cage moieties. The Fe(II) metalloligand retains an octahedral coordination environment of six proximal imidazolimine nitrogen atoms from the tripodal ligand L, while each Pd(II) centre is coordinated to four distal pyridyl nitrogens from four metalloligands to form square planar geometry.
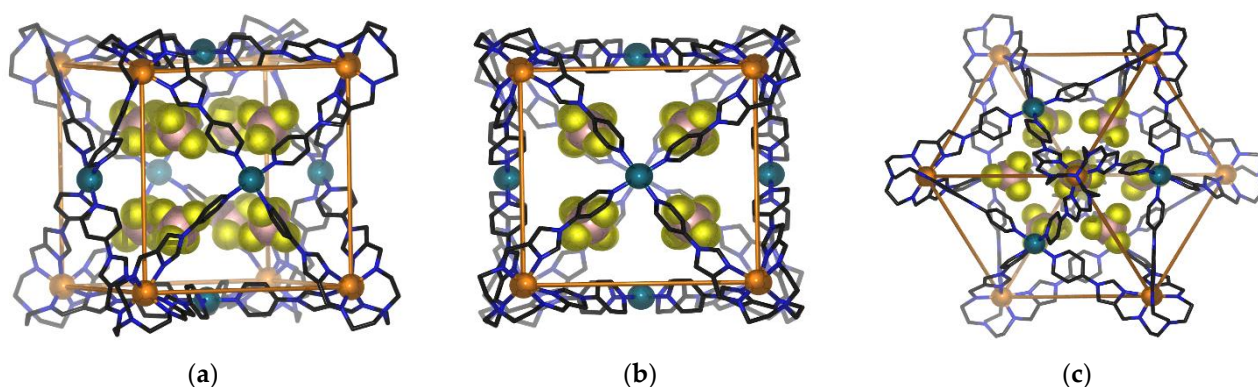


(**a**)  (**b**)  (**c**)

**Figure 5.** Schematic representation of the same view shown three ways for the single crystal X-ray diffraction structure of **1** encapsulating the $BF_4^-$ anions within the void; (**a**) offset edge view of **1** (**b**) $C_4$ axis view of **1**; (**c**) $C_3$ axis view of **1**. The $BF_4^-$ anions outside the cage, solvents and hydrogen atoms are not shown for clarity.

Eight Fe(II) centres from eight metalloligands define the corners of the cage, while six Pd(II) cations occupy the centres of the six faces to form overall a face-centred cubic geometry (Figure 5). All eight Fe(II) centres have distorted octahedral coordination geometries. Each of the Fe(II) coordination shells exhibit either Λ Λ Λ Λ Λ Λ Λ Λ or Δ Δ Δ Δ Δ Δ Δ Δ configurations, with equal numbers of both enantiomeric forms coexisting in the crystal lattice. The average Fe-N$_{imidazole}$ bond lengths at 100 K are 2.19 Å, with average octahedral

distortion parameters of $\Sigma = 131.3°$ (Table 2). These values are consistent with the presence of a HS Fe(II) coordination environment at 100K.

As discussed in the previous section, the metalloligand (**3**) crystal structure is in accordance with the magnetic data and indicates the presence of HS Fe(II) centres. The average coordinate bond length is 2.20 Å, and an $\Sigma$ value of 105° was calculated. The total difference of all coordinate bond lengths from the average value ($\zeta$) was 0.16 Å, and a trigonal projection distortion parameter ($\Theta$) of 280.4° was calculated.

The values of these structural parameters for each metalloligand change, as expected, upon reconformation of the metalloligand structure to form the face-centred cubic cage. The average coordinate bond length of the metalloligand in the cage structure drops slightly to 2.19 Å, corresponding to an almost negligible difference of less than 1%. The other length distortion parameters, $\zeta$ and $\Delta$, also decrease in the cage structure, giving final values of 0.11 Å and 0.000066, respectively; these values are in keeping with the Fe coordinate bonds in the cage structure deviating very little from the average value. Although the length distortion parameters all decreased, both angular distortion parameters increased markedly with $\Sigma = 131.3°$ and $\Theta = 374.1°$, corresponding to respective increases of approximately 25% and 33%. Together with the very small decrease in average coordinate bond length, the rise of angular distortions implies that the HS electronic state has been preserved in all Fe coordination sites in the cage structure. The sharp rise in the angular octahedral distortions in the cage compared to the metalloligand indicate a reconformation of the chelate rings relative to one another, which is assumed to be primarily driven by the realignment of the ligand "arms" when forming the face-centred cubic architecture.

The molecular volumes of the metalloligand motif in the structures of $FeL(BF_4)_2$ (**3**) and cage **1** were calculated and yielded values of 519.2 and 510.3 $Å^3$, respectively, corresponding to a decrease of 1.8%. This volume difference indicates some shrinkage of the metalloligand motif when adopting its final configuration in the cage structure. In order to compare the extent of the metalloligand conformational change in $FeL(BF_4)_2$ (**3**) and cage **1**, two additional structural parameters will now be discussed. The first is the angle between the binding axes of the pyridine moieties of each metalloligand. In an idealised face-centred cube structure, with respect to any corner of a cube, the angle between any two adjacent facial centres is 60 degrees. Therefore, it seems reasonable to assume that the angles between the bonding axes of the secondary donor sites should approximate this angle. The bonding axis of each pyridine binding domain (N-Pd bond) is close to being coaxial with the axis defined by the secondary pyridine donor and the C atom, which is positioned opposite in the pyridine ring (Figure 6). As such, for the sake of analytic consistency between the $FeL(BF_4)_2$ (**3**) and cage **1**, we opted to model the bonding axis as being colinear with the interval defined by two atoms in the ith pyridine domain, the distal N, and C opposite in the ring. The angle between the bonding axes for the metalloligand motifs was calculated for both the $FeL(BF_4)_2$ (**3**) and cage **1** structures (see Figure S9).

The mutual bond angles obtained for the metalloligand structure were 57.9, 58.8 and 52.2°, with an average value of 55.3°. In the cage-bound metalloligand, the calculated value of 61.3° was obtained, and due to the symmetry operations of the space group this value corresponds to the average of all such mutual bond axis angles in the cage structure. Some variation from the ideal value of 60° may be explained by small deviations from the defined bond axis, and the axis of the N-Pd bond, as well as the ligand arm's direction of approach towards the Pd centre being misaligned with respect to the Fe-Pd axis.

The second structural parameter based on the crystal data was the torsion angle about the $C_3$ axis (pseudo-$C_3$ in the case of the metalloligand), between the coordinating imine N and the distal secondary pyridyl-N on the same ligand arm ($N_{imine}$-Fe-centroid-$N_{pyridine}$), where the centroid was taken from the three distal pyridyl-N positions (Figure 7). This value was taken to represent the degree of twist manifested by the metalloligand. The torsion values found for $FeL(BF_4)_2$ were 50.0, 51.6 and 48.8°, with an average of 50.1°, while the same torsion angle measured for the symmetry equivalent ligand arms in the structure

of **1** was 55.4°. The degree of twist in the metalloligand upon adopting the face-centred cubic architecture is 10.6% higher than the average seen for FeL(BF$_4$)$_2$.
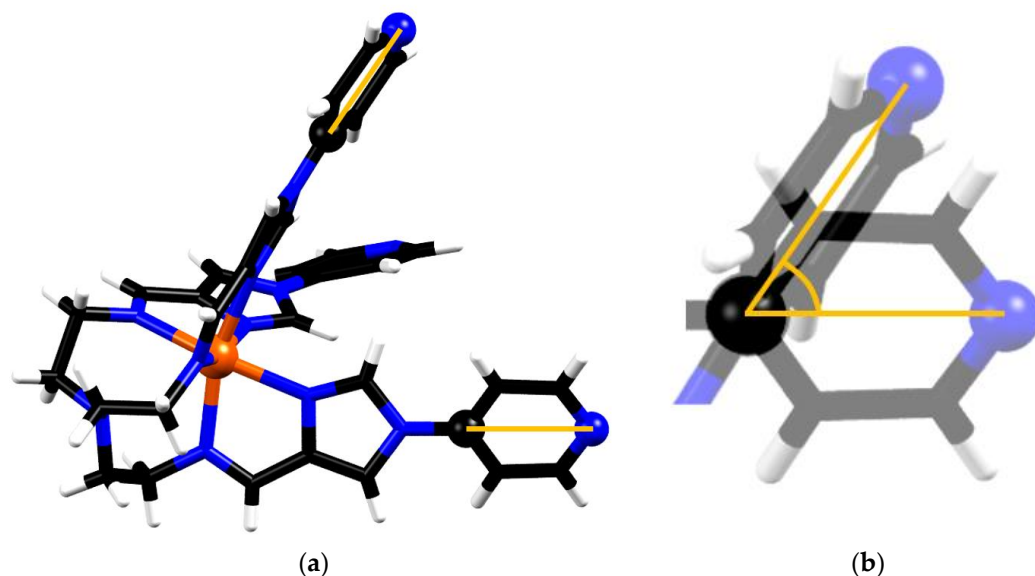


**Figure 6.** Representation of two selected mutually-positioned secondary group bonding axes in the metalloligand. (**a**) the intervals corresponding to the bonding direction of each of the secondary binding domains are highlighted, as defined by the coordinates of C9 and N4 in each arm of the metalloligand. (**b**) Since the bonding axes do not intersect, they are translated such that the reference C atoms in both ligand arms share the same point. The angle between axes can then be calculated.
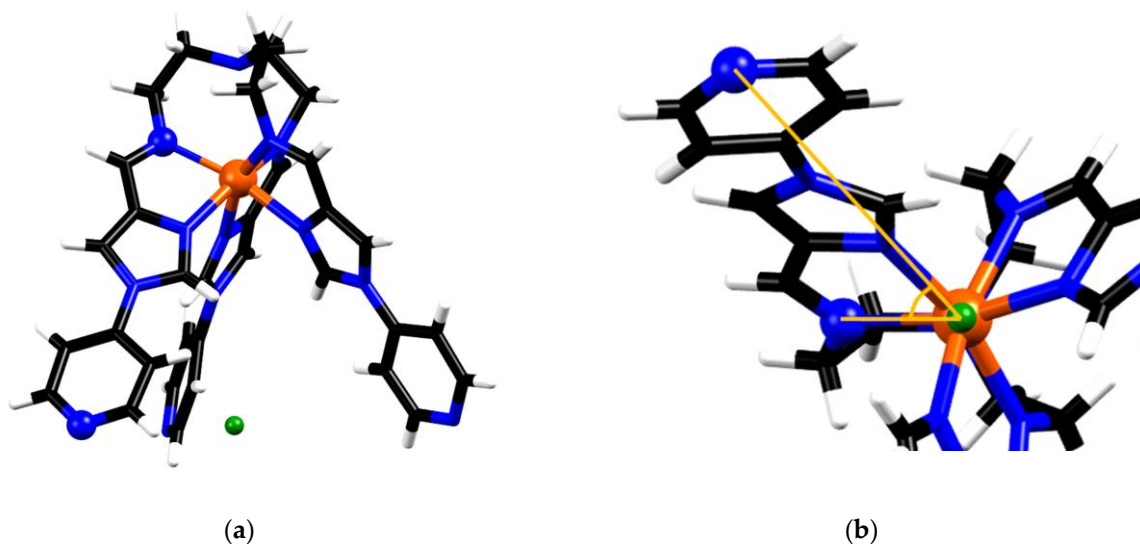


**Figure 7.** Schematic showing the torsion angles used to represent molecular twist, (**a**) highlights the chosen atoms (represented by balls) and the centroid between distal N's (green) (**b**) shows the torsion angle, as viewed along the pseudo threefold axis of the metalloligand in FeL$^{2+}$.

The formation of the face-centred cubic architecture forces the metalloligand to change conformation such that the final cubic structure is stable. The mutually positioned bonding axial angles ideally adopt a value close to 60° and large deviations from this value would not be conducive to cage formation. The reconformation of the ligand arms in each metalloligand is clearly an important feature in the formation of the final overall cubic structure. This motion of the ligand arms induces a greater degree of twist in each individual metalloligand in cage **1**, as compared to the situation in FeL(BF$_4$)$_2$ (**3**). It also induces adjustments in

the octahedral coordination sphere, leading to a decrease in the octahedral length distortion parameters, concomitant with a sharp rise in angular distortion parameters and, ultimately, the stabilization of the HS electronic state in the metalloligand units.

## 4. Conclusions

In this report, we discuss the self-assembly of a cubic $Fe_8$-$Pd_6$ heterobimetallic cage (**1**) obtained using the metalloligand approach. The commonly studied imidazolimine metal coordination moiety was incorporated in the tripodal $N_6$-donor (3-(((E)-(1-(pyridin-4-yl)-1H-imidazol-4-yl)methylene)amino)-N,N-bis(2-(((E)-(1-(pyridin-4-yl)-1H-imidazol-4-yl)methylene) amino)ethyl)propan-1-amine) ligand (**2**) whose weaker ligand field resulted in a new metalloligand (**3**) incorporating HS Fe(II) metal centres. Further coordination of Pd(II) to the secondary coordination sites of **3** (that is, the distal pyridyl groups) resulted in the formation of the heterobimetallic cationic cage $[Fe_8Pd_6L_8]^{28+}$. Both the $\Lambda$ and $\delta$ enantiomers of the cage **1** were found to crystallise in the *Fm-3c* crystal lattice. Despite significant reorientation of the metalloligand structure, the HS state of the Fe(II) centres was maintained following their occupancy of the eight corners of the discrete cubic architecture. The average metal-donor bond lengths and the octahedral distortion parameter ($\Sigma$) for the metalloligand, at 2.20 Å and 105.0°, respectively, for the heterobimetallic cage, were found to be 2.19 Å and 131.1°. This is in accordance with compression and further distortion of the coordination environment following coordination of the metalloligand's secondary donor groups to the Pd(II) centres. Furthermore, the tripodal metalloligands in cage **1** were found to decrease in volume in response to the secondary group bonding in forming the cubic architecture. The present study provides many interesting areas for future exploration. Changes in the identities of the metal centres will almost certainly allow the formation of related homo and heterometallic cages with predesigned structural and electronic natures, thus pointing the way towards the rational synthesis of new systems displaying a wide range of magnetic, optical, redox and other properties.

# References

1. McConnel, A.J. Metallosupramolecular cages: From design principles and characterisation techniques to applications. *Chem. Soc. Rev.* **2022**, *51*, 2957–2971. [CrossRef] [PubMed]
2. Hardy, M.; Lützen, A. Better Together: Functional Heterobimetallic Macrocyclic and Cage-like Assemblies. *Chem. Eur. J.* **2020**, *26*, 13332–13346. [CrossRef] [PubMed]
3. Chen, L.; Chen, Q.; Wu, M.; Jiang, F.; Hong, M. Controllable Coordination-Driven Self-Assembly: From Discrete Metallocages to Infinite Cage-Based Frameworks. *Acc. Chem. Res.* **2015**, *48*, 201–210. [CrossRef]
4. Clegg, J.K.; Li, F.; Lindoy, L.F. Di-, Tri- and Oligometallic Platforms: Versatile Components for Use in Metallo-Supramolecular Chemistry. *Coord. Chem. Rev.* **2013**, *257*, 2536–2550. [CrossRef]
5. Ward, M.D.; Raithby, P.R. Functional Behaviour from Controlled Self-Assembly: Challenges and Prospects. *Chem. Soc. Rev.* **2013**, *42*, 1619–1636. [CrossRef]
6. Young, N.J.; Hay, B.P. Structural Design Principles for Self-Assembled Coordination Polygons and Polyhedra. *Chem. Commun.* **2013**, *49*, 1354–1379. [CrossRef] [PubMed]
7. Li, F.; Lindoy, L.F. Metalloligand Strategies for Assembling Heteronuclear Nanocages—Recent Developments. *Aust. J. Chem.* **2019**, *72*, 731–741. [CrossRef]
8. Li, L.; Fanna, D.J.; Shepherd, N.D.; Lindoy, L.F.; Li, F. Constructing Coordination Nanocages: The Metalloligand Approach. *J. Incl. Phenom. Macrocycl. Chem.* **2015**, *82*, 3–12. [CrossRef]
9. Caulder, D.L.; Raymond, K.N. The Rational Design of High Symmetry Coordination Clusters. *J. Chem. Soc. Dalton Trans.* **1999**, 1185–1200. [CrossRef]
10. Fujita, M.; Umemoto, K.; Yoshizawa, M.; Fujita, N.; Kusukawa, K.; Biradha, K. Molecular paneling via Coordination. *Chem. Commun.* **2001**, 509–518. [CrossRef]
11. Zhang, D.; Ronson, T.K.; Nitschke, J.R. Functional Capsules via Subcomponent Self-Assembly. *Acc. Chem. Res.* **2018**, *51*, 2423–2436. [CrossRef] [PubMed]
12. Cook, T.R.; Stang, P.J. Recent Developments in the Preparation and Chemistry of Metallcycles and Metallacages via Coordination. *Chem. Rev.* **2015**, *115*, 7001–7045. [CrossRef] [PubMed]
13. Leninger, S.; Olenyuk, B.; Stang, P.J. Self-Assembly of Discrete Cyclic Nanostructures Mediated by Transition Metals. *Chem. Rev.* **2000**, *100*, 853–908. [CrossRef] [PubMed]
14. Chakrabarty, R.; Mukherjee, P.S.; Stang, P.J. Supramolecular Coordination: Self-Assembly of Finite Two- and Three-Dimensional Ensembles. *Chem. Rev.* **2011**, *111*, 6810–6918. [CrossRef] [PubMed]
15. Brown, C.J.; Toste, F.D.; Bergman, R.G.; Raymond, K.N. Supramolecular Catalysis in Metal–Ligand Cluster Hosts. *Chem. Rev.* **2015**, *115*, 3012–3035. [CrossRef]
16. Smulders, M.M.J.; Riddell, I.A.; Browne, C.; Nitschke, J.R. Building on Architectural Principles for Three-Dimensional Metallo-supramolecular Construction. *Chem. Soc. Rev.* **2013**, *42*, 1728–1754. [CrossRef]
17. Li, L.; Zhang, Y.; Avdeev, M.; Lindoy, L.F.; Harman, D.G.; Zhen, R.; Cheng, Z.; Aldrich-Wright, J.R.; Li, F. Self-assembly of a unique 3d/4f heterometallic square prismatic box-like coordination cage. *Dalton Trans.* **2016**, *45*, 9407–9411. [CrossRef]
18. Zhang, Y.-Y.; Gao, W.-X.; Lin, L.; Jin, G.-X. Recent Advances in the Construction and Applications of Heterometallic Macrocycles and Cages. *Coord. Chem. Rev.* **2017**, *344*, 323–344. [CrossRef]
19. Li, H.; Yao, Z.-J.; Liu, D.; Jin, G.-X. Multi-Component Coordination-Driven Self-Assembly toward Heterometallic Macrocycles and Cages. *Coord. Chem. Rev.* **2015**, *293–294*, 139–157. [CrossRef]
20. Bousseksou, A.; Molnár, G.; Real, J.A.; Tanaka, K. Spin Crossover and Photomagnetism in Dinuclear Iron(II) Compounds. *Coord. Chem. Rev.* **2007**, *251*, 1822–1833. [CrossRef]
21. Bousseksou, A.; Molnár, G.; Salmon, L.; Nicolazzi, W. Molecular Spin Crossover Phenomenon: Recent Achievements and Prospects. *Chem. Soc. Rev.* **2011**, *40*, 3313–3335. [CrossRef] [PubMed]
22. Hogue, R.W.; Singh, S.; Brooker, S. Spin Crossover in Discrete Polynuclear Iron(II) Complexes. *Chem. Soc. Rev.* **2018**, *47*, 7303–7338. [CrossRef] [PubMed]
23. McConnell, A.J. Spin-State Switching in Fe(II) Helicates and Cages. *Supramol. Chem.* **2017**, *30*, 858–868. [CrossRef]
24. Gütlich, P.; Gaspar, A.B.; Garcia, Y. Spin State Switching in Iron Coordination Compounds. *Beilstein J. Org. Chem.* **2013**, *9*, 342–391. [CrossRef] [PubMed]
25. Duriska, M.B.; Neville, S.M.; Moubaraki, B.; Cashion, J.D.; Halder, G.J.; Chapman, K.W.; Balde, C.; Lètard, J.; Murray, K.S.; Kepert, C.J.; et al. A Nanoscale Molecular Switch Triggered by Thermal, Light, and Guest Perturbation. *Angew. Chem. Int. Ed.* **2009**, *121*, 2587–2590. [CrossRef]
26. Li, L.; Saigo, N.; Zhang, Y.; Fanna, D.J.; Shepherd, N.D.; Clegg, J.K.; Zheng, R.; Hayami, S.; Lindoy, L.F.; Aldrich-Wright, J.R.; et al. A Large Spin-Crossover $[Fe_4L_4]^{8+}$ Tetrahedral Cage. *J. Mat. Chem. C.* **2015**, *3*, 7878–7882. [CrossRef]
27. Struch, N.; Bannwarth, C.; Ronson, T.K.; Lorenz, Y.; Mienert, B.; Wagner, N.; Engeser, M.; Bill, E.; Puttreddy, R.; Rissanen, K.; et al. An Octanuclear Metallosupramolecular Cage Designed to Exhibit Spin-Crossover Behavior. *Angew. Chem. Int. Ed.* **2017**, *56*, 4930–4935. [CrossRef]
28. Li, L.; Craze, A.R.; Mustonen, O.; Zenno, H.; Whittaker, J.J.; Hayami, S.; Lindoy, L.F.; Marjo, C.E.; Clegg, J.K.; Aldrich-Wright, J.R.; et al. A mixsed-spin spin-crossover thiozolylimine $[Fe_4L_6]^{8+}$ cage. *Dalton Trans.* **2019**, *48*, 9935–9938. [CrossRef]

29. Ferguson, A.; Squire, M.A.; Siretanu, D.; Mitcov, D.; Mathonière, C.; Clérac, R.; Kruger, P.E. A Face-Capped [Fe$_4$L$_4$]$^{8+}$ Spin Crossover Tetrahedral Cage. *Chem. Commun.* **2013**, *49*, 1597–1599. [CrossRef]

30. Bilbeisi, R.A.; Zarra, S.; Feltham, H.L.C.; Jameson, G.N.L.; Clegg, J.K.; Brooker, S.; Nitschke, J.R. Guest Binding Subtly Influences Spin Crossover in an Fe$^{II}_4$L$_4$ Capsule. *Chem. Eur. J.* **2013**, *19*, 8058–8062. [CrossRef]

31. Li, F.; Sciortino, N.F.; Clegg, J.K.; Neville, S.M.; Kepert, C.J. Self-Assembly of an Octanuclear High-Spin Fe$^{II}$ Molecular Cage. *Aust. J. Chem.* **2014**, *67*, 1625–1628. [CrossRef]

32. Hardy, M.; Struch, N.; Holstein, J.J.; Schnakenburg, G.; Wagner, N.; Engeser, M.; Beck, J.; Clever, G.H.; Lützen, A. Dynamic Complex-to-Complex Transformations of Heterobimetallic Systems Influence the Cage Structure or Spin State of Iron(II) Ions. *Angew. Chem. Int. Ed.* **2020**, *59*, 3195–3200. [CrossRef] [PubMed]

33. McConnell, A.R.; Aitchison, C.M.; Grommet, A.B.; Nitschke, J.R. Subcomponent Exchange Transforms an Fe$^{II}_4$L$_4$ Cage from High- to Low-Spin, Switching Guest Release in a Two-Cage System. *J. Am. Chem. Soc.* **2017**, *139*, 6294–6297. [CrossRef] [PubMed]

34. Miller, T.F.; Holloway, L.R.; Nye, P.P.; Lyon, Y.; Beran, G.J.O.; Harman, W.H.; Julian, R.R.; Hooley, R.J. Small Structural Variations Have Large Effects on the Assembly Properties and Spin State of Room Temperature High Spin Fe(II) Iminopyridine Cages. *Inorg. Chem.* **2018**, *57*, 13386–13396. [CrossRef]

35. Craze, A.R.; Bhadbhade, M.M.; Komatsumaru, Y.; Marjo, C.E.; Hayami, S.; Li, F. A Rare Example of a Complete, Incomplete, and Non-Occurring Spin Transition in a [Fe$_2$L$_3$]X$_4$ Series Driven by a Combination of Solvent-and Halide-Anion-Mediated Steric Factors. *Inorg. Chem.* **2020**, *59*, 1274–1283. [CrossRef]

36. Craze, A.; Bhadbhade, M.; Kepert, C.; Lindoy, L.; Marjo, C.; Li, F.; Craze, A.R.; Bhadbhade, M.M.; Kepert, C.J.; Lindoy, L.F.; et al. Solvent Effects on the Spin-Transition in a Series of Fe(II) Dinuclear Triple Helicate Compounds. *Crystals.* **2018**, *8*, 376. [CrossRef]

37. Craze, A.R.; Sciortino, N.F.; Badbhade, M.M.; Kepert, C.J.; Marjo, C.E.; Li, F. Investigation of the Spin Crossover Properties of Three Dinulear Fe(II) Triple Helicates by Variation of the Steric Nature of the Ligand Type. *Inorganics.* **2017**, *5*, 62. [CrossRef]

38. Cowieson, N.P.; Aragao, D.; Clift, M.; Ericsson, D.J.; Gee, C.; Harrop, S.J.; Mudie, N.; Panjikar, S.; Price, J.R.; Riboldi-Tunnicliffe, A.; et al. MX1: A bending-magnet crystallography beamline serving both chemical and macromolecular crystallography communities at the Australian Synchrotron. *J. Synchrotron Rad.* **2015**, *22*, 187–190. [CrossRef]

39. Kabsch, W. XDS. Automatic processing of rotation diffraction data from crystals of initially unknown symmetry and cell constants. *J. Appl. Crystallogr.* **1993**, *26*, 795–800. [CrossRef]

40. *SADABS*, version 2014/5; Bruker AXS Inc.: Madison, WI, USA, 2001.

41. Sheldrick, G.M. *SHELXT—Integrated space-group and crystal-structure determination. Acta. Cryst. A* **2015**, *71*, 3–8. [CrossRef]

42. Sheldrick, G.M. *SHELX-2014: Programs for Crystal Structure Analysis*; University of Göttingen: Göttingen, Lower Saxony, Germany, 2014.

43. Sheldrick, G.M. Crystal structure refinement with SHELXL. *Acta. Cryst. C* **2015**, *71*, 3–8. [CrossRef] [PubMed]

44. Dolomanov, O.V.; Bourhis, L.J.; Gildea, R.J.; Howard, J.A.K.; Puschmann, H. OLEX2: A complete structure solution, refinement and analysis program. *J. Appl. Cryst.* **2009**, *42*, 339–341. [CrossRef]

45. Che, C.; Li, S.; Yang, B.; Xin, S.; Yu, Z.; Shao, T.; Tao, C.; Lin, S.; Yang, Z. Synthesis and characterization of Saint-75 derivatives as Hedgehog-pathway inhibitors. *Beilstein J. Org. Chem.* **2012**, *8*, 841–849. [CrossRef] [PubMed]